



Influence of Sn content on microstructure and electrochemical properties of Sn–NiTi film anodes in lithium ion batteries



Renzong Hu, Hui Liu, Meiqin Zeng, Jiangwen Liu, Min Zhu*

Guangdong Key Laboratory of Advanced Materials for Energy Storage, School of Materials Science and Engineering, South China University of Technology, Guangzhou 510640, China

HIGHLIGHTS

- Sn–NiTi films with different Sn contents were deposited on Cu by co-sputtering.
- The NiTi–20.2%Sn film had micro-sized Sn dispersed in porous amorphous NiTi matrix.
- Nanocrystalline Ni_3Sn_4 formed and surrounded outside the Sn in NiTi–39%Sn film.
- The NiTi–39%Sn film yielded better performance due to the existence of Ni_3Sn_4 .

ARTICLE INFO

Article history:

Received 16 October 2012

Received in revised form

15 November 2012

Accepted 23 November 2012

Available online 30 November 2012

Keywords:

Lithium ion battery

Tin anode

Amorphous nickel titanium alloy

Irreversible capacity

ABSTRACT

Sn–NiTi composite thin films consisting of different amounts of Sn, prepared by directly co-sputtering pure Sn and NiTi alloy, have been characterized as anodes for lithium ion batteries. The composite films with relative low Sn content (20.2, 25.2 wt%) had a microstructure of micro-sized Sn particles uniformly dispersed in the porous α -NiTi matrix. In contrast, in the film with a higher Sn content (39.0 wt%), a part of the Sn reacted with NiTi to form Ni_3Sn_4 intermetallic surrounding the Sn. The inactive NiTi covered and protected most of the surface of Sn in these composite films and resulted in quite low initial irreversible capacity losses and greatly enhanced cycle performances. The results showed that the Sn–NiTi film with 39.0 wt% Sn delivered higher reversible capacity and superior capacity retention, which was attributed to the interfacial reaction between Sn and NiTi phases, as well as the good electrochemical reversibility of nanocrystalline Ni_3Sn_4 formed in NiTi matrix.

© 2012 Elsevier B.V. All rights reserved.

1. Introduction

Li-ion batteries (LIBs) are key power sources in various portable electronic devices, medical implants and electric vehicles due to their high energy density and power density, long lifespan and flexible design [1]. However, the available graphite-based anodes in commercial batteries have an obvious disadvantage in terms of their limited capacity ($372 \text{ mAh g}^{-1}/837 \text{ mAh cm}^{-3}$). Thus, replacing graphite with materials of higher specific capacities is an attractive route to develop a new generation LIBs that offer higher performance [2]; metallic Sn has been envisioned as a promising anode material due to its high theoretical capacity of $993 \text{ mAh g}^{-1}/7262 \text{ mAh cm}^{-3}$ in the range of moderate to safe operating potentials (0.8–0.3 V vs. Li) [3,4]. However, the main limitation to this high capacity anode is an accompanying volumetric expansion of up to 250% in the lithiation of the crystalline Sn, which results in

poor cyclic performance due to pulverization and delamination of the electrode structure [5–7].

In order to improve the cyclic performance of Sn-based anodes, a variety of complicated methods have been used to prepare Sn–(M)–C nanocomposite anodes in which a dispersion of nanosized Sn particles are embedded in an amorphous carbon matrix that acts as a buffer to tolerate the mechanical stress from the volume change of the Sn phases; extensive studies have achieved an enhanced cyclic performance of Sn-based electrodes [8–18]. However, the deformation of the carbon matrix is not recoverable, and thus the buffering effect is limited and only adequate for small expansions of a low content of nanosized Sn particles, but not for Sn particles with sizes in the microscale range or larger. Even worse, there are very large initial irreversible losses of capacity ($200\text{--}600 \text{ mAh g}^{-1}$) in these Sn–C composite electrodes [10–14,16,18]. These losses are due to unavoidable Li trapping in the amorphous carbon and solid-electrolyte interfacial (SEI) layer formation on the carbon matrix surface, as well as other irreversible Li-consuming reactions. Thus, it is very important to reduce this initial

* Corresponding author. Tel.: +86 20 87113924; fax: +86 20 87111317.
E-mail address: memzhu@scut.edu.cn (M. Zhu).

irreversible capacity loss and to improve the cyclic performance and high-rate capability by replacing the carbon matrix with other appropriately inactive materials.

Recently, we reported that the initial irreversible capacity loss of Sn-based electrodes could be dramatically reduced and a good cyclic performance achieved by replacing the carbon matrix with amorphous-NiTi and B2/B19'-NiTi shape memory alloy matrix [19,20]. Jung et al. also reported that the supported Ni–Ti alloy matrix can greatly enhance the cycle performance of the nanosized Si anode [21]. In our previous work, an Sn–NiTi composite film embedded with micro-sized ($\sim 0.2 \mu\text{m}$) Sn in an amorphous NiTi matrix was prepared by co-sputtering of pure Sn and NiTi alloy, in which the amorphous NiTi matrix protected the surface of the Sn particles well and effectively accommodated the volume change resulting from the Li–Sn reactions [19]. However, the Sn content in that Sn–NiTi composite electrode was relatively low, only about a quarter of the total weight of the Sn–NiTi composite layer, which led to quite a low specific capacity in the electrode if the weight of the inactive NiTi matrix was taken into account. Thus, it is now necessary to explore Sn–NiTi composites with higher Sn content to attain a higher specific capacity of film electrode. However, the influence of higher Sn content on the microstructure and electrochemical performance of Sn–NiTi composite film anodes has not been previously investigated and this is the main objective of the present work.

2. Experimental

2.1. Preparation of Sn–NiTi composite film electrodes

The Sn–NiTi composite film was fabricated by co-sputtering Ni50Ti50 (at.%) and pure Sn (99.99%) targets onto a Cu foil substrate, using a KYKY JGB-560 high-vacuum magnetron sputtering system at room temperature. During deposition, the substrate holder was rotated at a speed of 30 rpm in order to minimize the inhomogeneity of the composite. The film was deposited after a base pressure of 2.0×10^{-4} Pa was achieved. Argon (purity $\geq 99.999\%$) at 1.0 Pa was used as the working gas during deposition. The NiTi target was sputtered using a radio frequency magnetron and the Sn target was sputtered by a direct current magnetron, which is similar to that for the deposition of Sn–NiTi composite film (named as Sn–NiTi-1, 150 W for NiTi and 60 W for Sn with 0.5 Pa Ar as working gas) reported in Ref. [19]. However, different sputtering powers were applied to prepare two other Sn–NiTi composite films: NiTi (300 W) and Sn (60 W) for Sn–NiTi-2, and NiTi (300 W) and Sn (100 W) for Sn–NiTi-3. The amount of deposited materials on the Cu foil was determined by weighing the film before and after sputtering deposition using an FA1104N balance.

2.2. Electrochemical measurement

The electrochemical performance of the thin film electrodes was investigated with CR2016 coin-type half-cells assembled in an argon-filled glove box. The as-deposited thin films were used directly as working electrodes. Li ribbon and polyethylene membrane (Teflon® Gold LP) were the counter electrode and separator, respectively. The electrolyte was LiPF₆ (1 mol L^{-1}) in a mixture of ethylene carbonate/diethyl carbonate/ethyl methyl carbonate (1:1:1 by volume, Guangzhou Tinci High-Tech Material Co. Ltd.). Galvanostatic charge–discharge tests were conducted on BT2000 (Arbin Instruments, USA) and CT2001A (LAND, China) battery testers at different current densities over the voltage range 0.01–1.5 V at room temperature. The specific charge/discharge capacities of the film electrodes were calculated with respect to the weight of Sn rather than the total mass of the deposited films.

2.3. Material characterization

The structures and morphologies of the as-prepared film samples were characterized using a Philips X-ray diffractometer (XRD) with Cu-K α radiation, a Carl Zeiss Supra 40 field emission scanning electron microscope (SEM), and a JEOL JEM-2100 transmission electron microscope (TEM) operating at 200 kV. The TEM specimens were prepared with a Gatan precision ion polishing system. The composition of the samples was determined by an INCA energy dispersive spectroscope attached to the SEM.

3. Results and discussion

3.1. Microstructure of the Sn–NiTi film electrodes

Fig. 1 shows the XRD patterns of the three Sn–NiTi composite films. It can be seen from Fig. 1(a) and (b) that the diffraction pattern of the Sn–NiTi-2 (Fig. 1(b)) is very similar to that of the Sn–NiTi-1 (Fig. 1(a)), in which the obvious peaks at 30.6, 32.0, 43.9, and 44.9° can be assigned without doubt to tetragonal Sn, indicating that the Sn–NiTi-2 and Sn–NiTi-1 films contained the crystalline Sn phase. There is no obvious peak that could be indexed to intermetallic phases in Ni–Ti, Sn–Ni, and Sn–Ti systems such as TiNi, Ti₂Ni, Ni₃Ti, Ni₃Sn₄, SnTi₂, suggesting that there was no appreciable reaction between Sn and NiTi during the sputtering process of Sn–NiTi-1 and Sn–NiTi-2 films using low sputtering power (60 W) for Sn, and that the film was composed of crystalline Sn and amorphous NiTi phase. However, for the Sn–NiTi-3 film shown in Fig. 1(c), in addition to the pure Sn phase, an obvious Ni₃Sn₄ intermetallic phase was detected in the film, suggesting that a part of Sn reacted with the NiTi during the sputtering process of Sn–NiTi film because the deposition temperature was high and the Sn even melted under the higher sputtering power (100 W).

Fig. 2(a–c) shows the back-scattered SEM images of the three Sn–NiTi composite films. The Sn content in the Sn–NiTi-1, Sn–NiTi-2 and Sn–NiTi-3 composite film was 20.2, 25.2 and 39.0 wt% respectively, as determined by EDS coupled with SEM. The detailed EDS analysis also indicated that the bright zones in Sn–NiTi-1 and Sn–NiTi-2 had much higher Sn contents than the gray zones. Taking into account the EDS and XRD results, as indicated by arrows in Fig. 2(a) and (b), the bright zones were mainly pure Sn phase while the gray zones were the NiTi matrix containing a lot of small Sn particles, as will be revealed by the TEM observation below. It

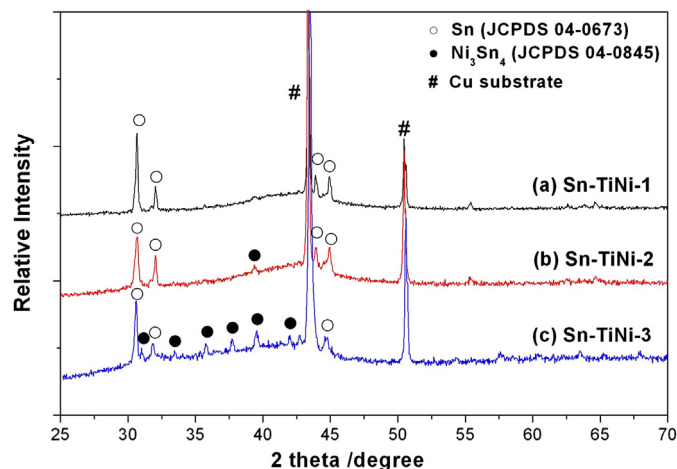


Fig. 1. X-ray diffraction patterns of the as-sputtered (a) Sn–NiTi-1, (b) Sn–NiTi-2, and (c) Sn–NiTi-3 composite film on Cu foil substrates.

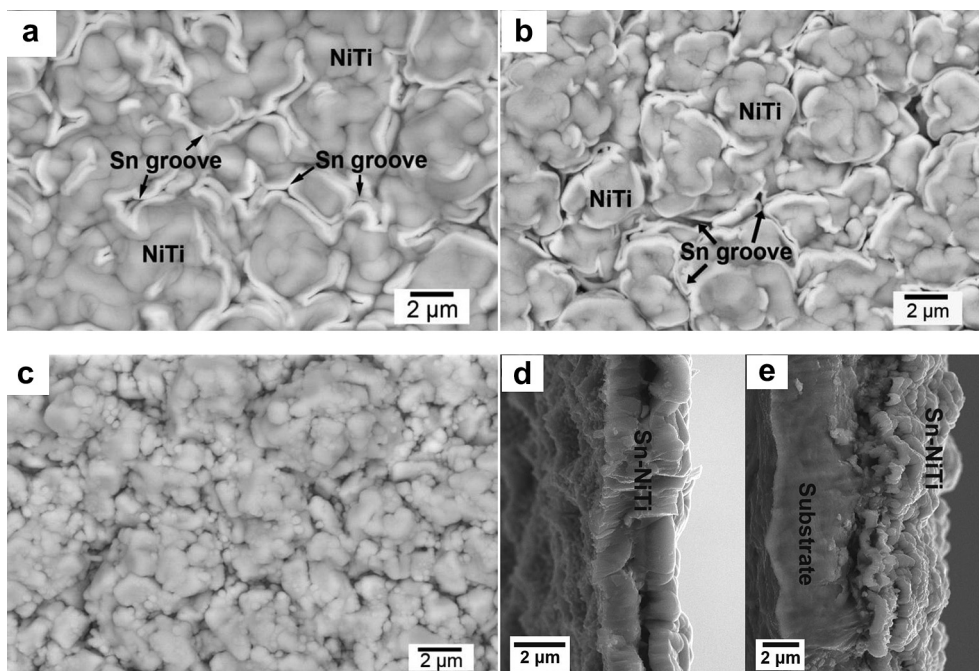


Fig. 2. Scanning electron micrographs of the (a) Sn–NiTi-1, (b) Sn–NiTi-2, and (c) Sn–NiTi-3 composite film; (d) and (e) the cross-sectional images of the Sn–NiTi-1 and Sn–NiTi-3 layers, respectively (in the former, the Sn–TiNi-1 having been peeled from the Cu substrate).

should be noted that the Sn and NiTi were co-deposited. However, as shown in the SEM images in Fig. 2(a) and (b), there were obvious interfaces between the Sn and the NiTi matrix. The Sn phase was mainly congregated in the gaps between NiTi zones, among which there were many deep grooves. This part of the Sn phase is thought to be softened Sn extruded from the NiTi matrix under the action of gravity and the internal stress generated during film growth. However, as shown in Fig. 2(c), the Sn–NiTi-3 film presented quite a different surface morphology in comparison with those of the Sn–NiTi-1 and Sn–NiTi-2, as no Sn grooves and interfaces between Sn and NiTi matrix were detectable on its surface. Fig. 1(d) and (e) shows SEM images of a fractured cross-section of the Sn–TiNi-1 and Sn–NiTi-3 films, respectively, in which the Sn–TiNi-1 was peeled from the Cu substrate. The thickness of the sputtered composite layers in the films was about 3.0 μm and they contained many micro-sized grooves and pores. These deep grooves and pores should be advantageous for improving the electrochemical performance of these Sn–NiTi film electrodes as the porous structure can tolerate quite high strain and be beneficial for lithium insertion/extraction.

TEM observations were carried out to investigate the dispersion and dimension of the Sn phases inside the NiTi matrix in each composite film. As shown in Fig. 3(a–c), Sn particles (dark zones) with different morphologies and different diameters, were dispersed in the NiTi matrix (bright zones). The Sn particles in the Sn–NiTi-1 film (Fig. 3(a)), of about 0.2 μm diameter, had nearly polyhedral shape, while there were larger Sn particles (about 0.5 μm) with anomalous shapes in the Sn–NiTi-2 film with a slightly higher Sn content. The characteristics of the single crystal Sn particles and the amorphous nature of the NiTi matrix in the two composite films were confirmed by their selected area electron diffraction patterns, shown as insets in Fig. 3(a). Furthermore, in these two films, there were obvious boundaries between the single crystal Sn particles and the amorphous NiTi (*a*-NiTi) matrix, which is consistent with the XRD results (Fig. 1(a) and (b)), showing that there was little solid reaction between the pure Sn and NiTi matrix

in the Sn–NiTi-1 and Sn–NiTi-2 composite films. With respect to the Sn–NiTi-3 film shown in Fig. 3(c), it can be seen that the Sn particles in the NiTi matrix were spherical but that there were no clear interfaces between the Sn and NiTi matrix. Instead, there were quite large Sn–Ni–Ti transition layers of different Sn content between the Sn particles and NiTi matrix. EDS (in TEM) analysis indicated that the Sn content at points A, B, and C labeled in Fig. 3(c) was 57.4, 43.2, and 17.7 wt%, respectively. The high resolution TEM image of area C shown in Fig. 3(d) clearly revealed that there were many Ni_3Sn_4 nanocrystals (about 10 nm) dispersed in the amorphous NiTi matrix, which is consistent with the XRD result (Fig. 1(c)) that a part of Sn reacted with NiTi to form Sn–Ni intermetallic phases during the co-sputtering process of the Sn–NiTi-3 film with higher Sn content. It should be noted that, actually, the amorphous NiTi was the dominant phase and made up most of the mass in region C. And thus the measured weight percent of Sn in region C (~17.7 wt%) was much lower than that of pure Ni_3Sn_4 phase (~57 wt%).

The combination of the above XRD, SEM, and TEM results thus proved that the co-sputtered Sn–NiTi composite films had different microstructures due to their different Sn contents, as shown schematically in Fig. 4. The structures of the films with relatively low Sn content (such as 20.2, 25.2 wt%) involved micro-sized Sn particles uniformly dispersed in the porous *a*-NiTi matrix, as shown in Fig. 4(a), in which there were many micro-sized Sn grooves connected to the surface of the film with micro-sized Sn particles within. However, in the film with relative higher Sn content (39.0 wt% Sn), as shown in Fig. 4(b), a part of Sn reacted with NiTi to form Ni_3Sn_4 intermetallic surrounding the Sn during the co-sputtering process of the film. Nevertheless, the NiTi covered most of the surface of both kinds of thin films. It is anticipated that the covering of inactive NiTi effectively accommodates the volume change of Li–Sn reactions and also protects the surface of the Sn particles in the electrolyte environment. However, the two kinds of Sn–NiTi thin films would present different anode behaviors due to their different Sn contents and the consequent different

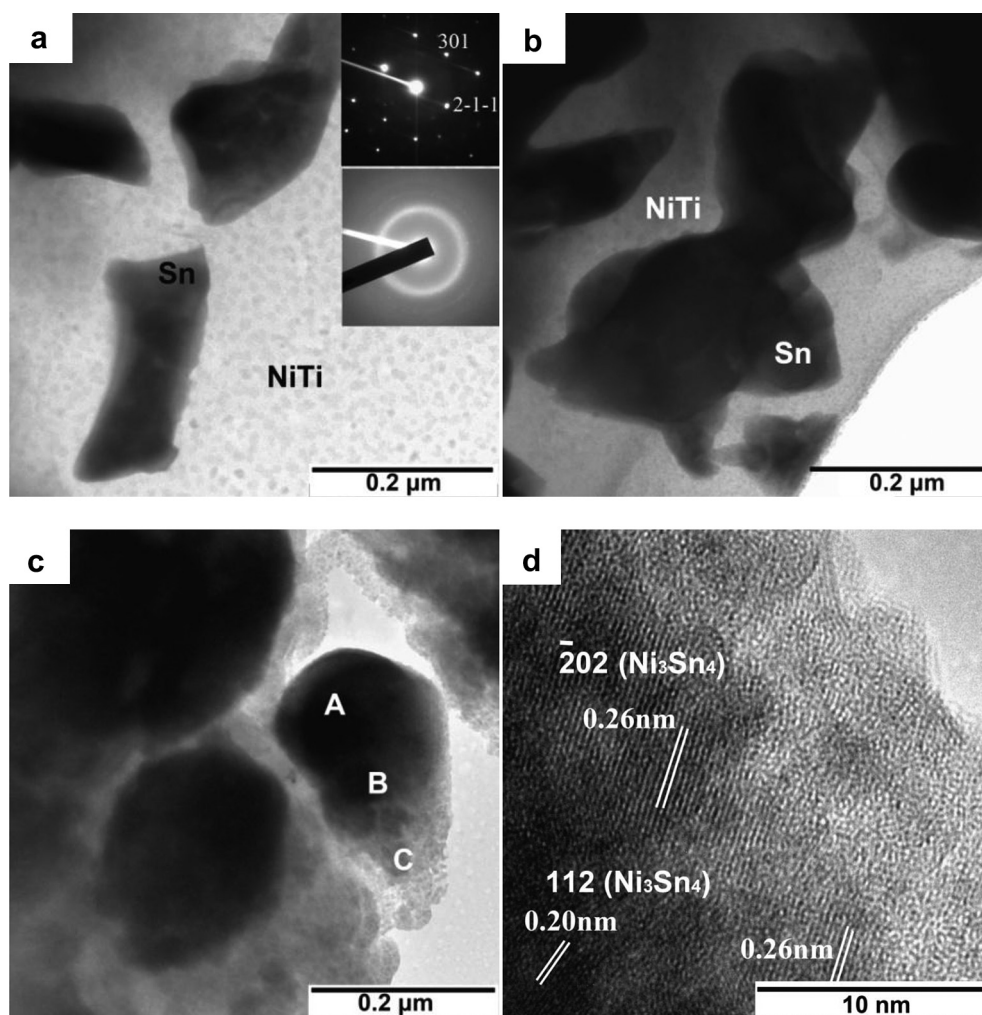


Fig. 3. Plane-view transmission electron microscopy (TEM) images of the (a) Sn–NiTi-1, (b) Sn–NiTi-2, and (c) Sn–NiTi-3 films; (d) high resolution TEM image for zone C marked in (c); insets in top right corner of (a) are selected area diffraction patterns for the single crystalline Sn and amorphous NiTi matrix.

microstructures. Especially, the nanocrystalline Ni_3Sn_4 had been confirmed to have excellent electrochemical reversibility and deliver high Li storage capacity [22,23], which should be beneficial to the enhancement of anode performance for Sn–NiTi-3 film. To confirm this, the electrochemical performance of the Sn–NiTi composite thin film electrodes was examined and the results are described below.

3.2. Electrochemical performance of the Sn–NiTi film electrodes

Fig. 5(a–c) exhibits the voltage profiles over the first 10 cycles at a current of 0.2 mA cm^{-2} for the Sn–NiTi-1, Sn–NiTi-2, and Sn–NiTi-3 film electrodes, respectively. It can be seen that all the first discharge curves of the film electrodes dropped rapidly to potential plateaus below 0.4 V vs. Li/Li^+ , which is different behavior from that

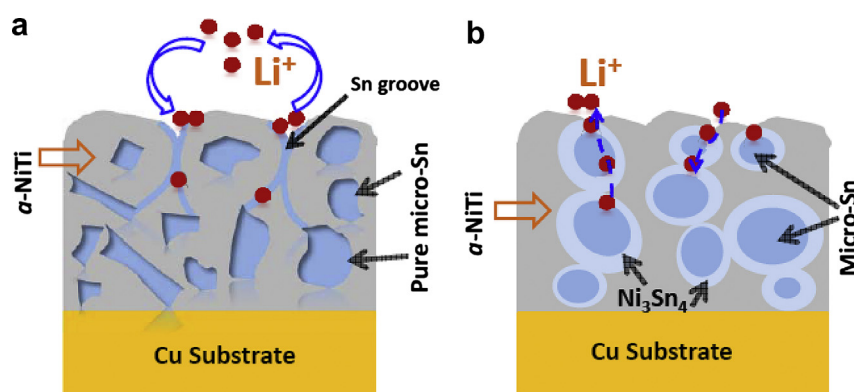


Fig. 4. Schematic microstructure of the Sn–NiTi composite film electrode (a) with low Sn content, and (b) with high Sn content.

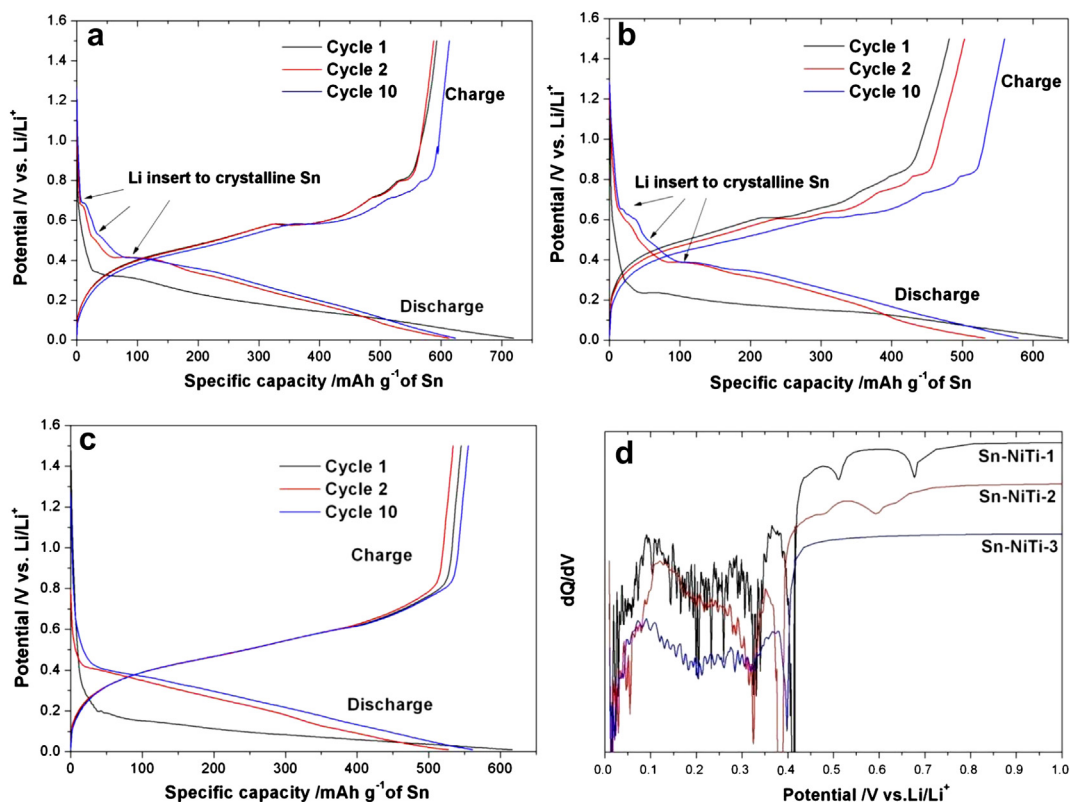


Fig. 5. Voltage profiles of the first, second and tenth cycle at a current of 0.2 mA cm^{-2} for (a) Sn–NiTi-1, (b) Sn–NiTi-2, and (c) Sn–NiTi-3 film electrode; (d) the derivatives for the second discharge profiles of the three electrodes.

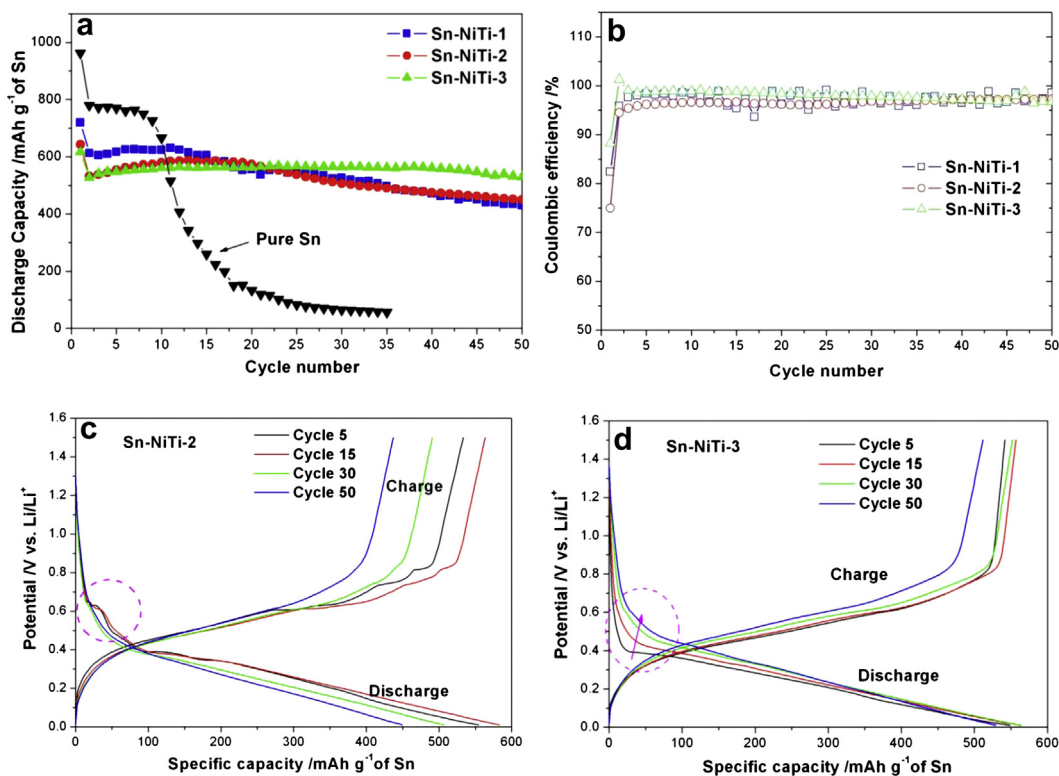


Fig. 6. (a) Comparison of the cycling performances of pure Sn and the three Sn–NiTi composite film electrodes at a current of 0.2 mA cm^{-2} ; (b) coulombic efficiency; (c) and (d) the discharge–charge profiles of representative cycles for Sn–NiTi-2 and Sn–NiTi-3, respectively.

of the second and subsequent cycles for the three electrodes. This is suggested to be due to the potential polarization of electrodes induced by the inactive NiTi layer covering the Sn phase which delayed the electrolyte (Li^+) reaching and reacting with the Sn particles inside during the initial discharge steps. However, as shown in Fig. 5(a) and (b), from the second cycle, potential onsets and multi-plateaus between 0.8 and 0.45 V vs. Li/Li^+ , which resulted from Li inserting in the crystalline Sn, are clear to see in the Sn–NiTi-1 and Sn–NiTi-2 film electrodes. By contrast, as shown in Fig. 5(c), the Sn–NiTi-3 electrode presented only a long potential plateau below 0.45 V vs. Li/Li^+ in the second and the tenth discharge curves, which may be due to Li mainly reacting with the Ni_3Sn_4 intermetallic phase [23,24]. These findings suggest that there are different reactants with Li in the film electrodes with low Sn content (Sn–NiTi-1 and Sn–NiTi-2) compared with higher Sn content (Sn–NiTi-3). The difference in anode behaviors of the two kinds of electrodes were further confirmed by the derivatives of the second discharge profiles of the three electrodes, as shown in Fig. 5(d). It is clear that there were obvious cathode peaks among the 0.8–0.45 V potential range which were induced by Li reacting with Sn in the Sn–NiTi-1 and Sn–NiTi-2 electrodes. However, there were no cathode peaks above 0.45 V vs. Li/Li^+ for the Sn–NiTi-3 electrode, indicating that the reaction of Li with pure Sn was absent in the initial 10 cycles in the Sn–NiTi-3 film. Furthermore, the second and the following cycle profiles were both similar and smooth, while the same sloping plateaus at lower potentials were due to the reversible lithiation reactions of nanocrystalline Ni_3Sn_4 [23].

Fig. 6(a) shows a comparison of the cyclic performances for the three Sn–NiTi composite film anodes with the pure Sn film between 0.01 and 1.5 V at a current of 0.2 mA cm^{-2} . It is clear to that all of these Sn–NiTi composite films had much better cycling abilities than the pure Sn film anode. They suffered an initial capacity loss of about 100 mAh g^{-1} for the first cycle; however, they presented quite different capacity retention trends as the number of cycles increased, due to their different Sn content and the accompanying different microstructures. With respect to the Sn–NiTi-1 and Sn–NiTi-2 anodes with low Sn content, the discharge capacity remained relative stable during the initial 15 cycles. Thereafter, however, the capacity gradually decreased to about 430 mAh g^{-1} as the cycling was extended to 50 times. In marked contrast, the Sn–NiTi-3 anode with higher Sn content of 39.0 wt% showed excellent cycling ability, although with a slightly lower initial discharge capacity. It delivered a capacity of 530 mAh g^{-1} after 50 cycles, without any noticeable fading of capacity. The excellent cycling ability is a clear indication that the mechanical integrity of the Sn–NiTi-3 film electrode was fully maintained and that the electrode could be repeatedly cycled without degradation. This, in turn, demonstrated that the α -NiTi conductive matrix in the Sn–NiTi-3 effectively buffered the volume expansion of the 39.0 wt% of Sn even though this Sn content was much larger than in the Sn–NiTi-1 and Sn–NiTi-2 electrodes. This may be attributed to the Ni_3Sn_4 intermetallic layers surrounding the pure Sn in the Sn–NiTi-3 electrode as shown in Figs. 3(c) and 4(b); it is due to this that the Ni_3Sn_4 layers provided strong interface binding between the Sn and the NiTi matrix to prevent the Sn particles from falling out. It needs to be noted that the excellent electrochemical reversibility of the nanocrystalline Ni_3Sn_4 should also be much beneficial to this good cycle performance in the Sn–NiTi-3 anode. Additionally, as shown in Fig. 6(b), the Sn–NiTi-3 had the highest initial coulombic efficiency of 88.2%, while the lowest value of 75% was yielded by the Sn–NiTi-2 anode, implying an initial irreversible capacity of 72 mAh g^{-1} for Sn–NiTi-3 and 160 mAh g^{-1} for Sn–NiTi-2. Nevertheless, the initial irreversible capacity losses in these Sn–NiTi electrodes were much lower than those of the reported

Sn–C nanocomposites (more than 400 mAh g^{-1}) [10–14,16,18]. This could be attributed to the covering α -NiTi matrix being inactive with respect to Li and electrolyte and thus there being less Li-consuming irreversible reaction on the surface of the α -NiTi. In particular, as shown in Figs. 2(c) and 4(b), there was only a very small amount of active Sn directly exposed on the surface of the Sn–NiTi-3 film electrode, leading to little SEI layer being formed on the Sn surface, resulting in the lowest initial irreversible capacity loss.

Fig. 6(c) and (d) shows the discharge–charge profiles at 0.2 mA cm^{-2} of a few representative cycles, namely cycles 5, 15, 30, and 50 for the Sn–NiTi-2 and Sn–NiTi-3 thin films, respectively. As indicated by arrows in Fig. 6(c), the potential plateaus induced by Li–Sn alloying near 0.6 and 0.4 V vs. Li/Li^+ disappeared in the Sn–NiTi-2 (also in the Sn–NiTi-1) anode as the cycling increased, suggesting the existence of nanocrystallization for the micro-sized Sn, and/or the loss of active pure Sn due to the Li-insertion induced volume expansion, which was responsible for the obvious fading in capacity after 15 cycles in the Sn–NiTi-1 and Sn–NiTi-2 electrodes. However, the voltage trend in Sn–NiTi-3 film was retained for all cycles, confirming the good reversibility of the reactions at the electrode. Furthermore, as indicated in the area circled in Fig. 6(d), the onset potential for lithiation increased from 0.4 to 0.65 V after 50 cycles. The onset potential of around 0.4 V vs. Li/Li^+ resulted from the electrochemical reaction of Ni_3Sn_4 , involving the formation of the $\text{Li}_{4.4}\text{Sn}$ alloy and the separation of Ni [24], whereas the

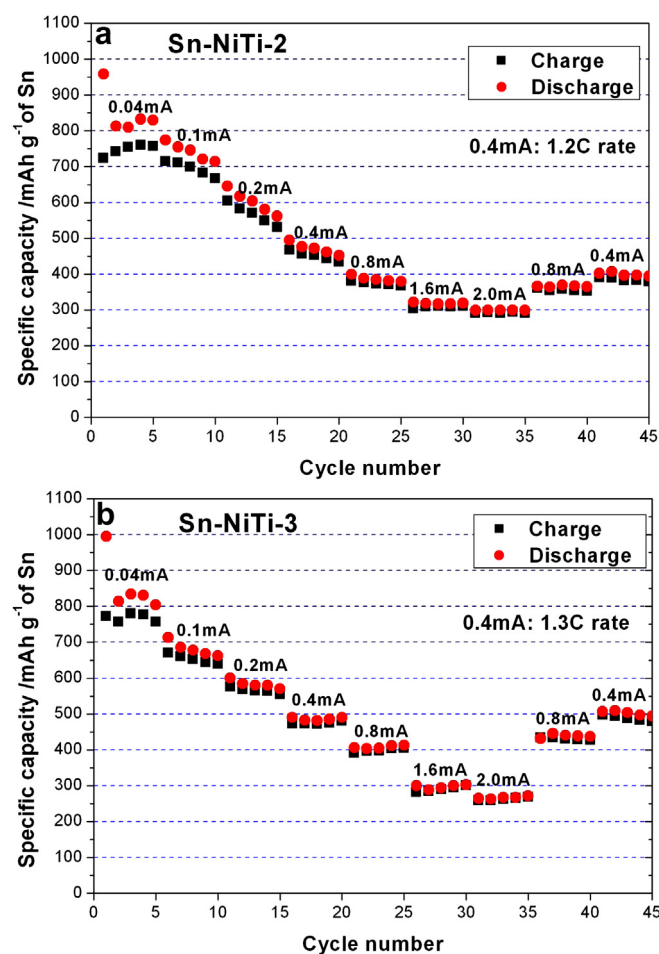


Fig. 7. Various C-rates performances of the Sn–NiTi composite film electrodes. Cut-off potential: 0.01–1.5 V vs. Li/Li^+ , (a) Sn–NiTi-2, 0.4 mA cm^{-2} corresponds to 1.2 C rate; (b) Sn–NiTi-3, 0.4 mA cm^{-2} corresponds to 1.3 C rate.

